Energy 308 (2024) 132853

Contents lists available at ScienceDirect

Energy

journal homepage: www.elsevier.com/locate/energy

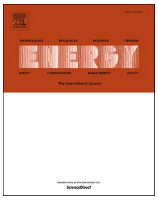

A novel fuel cell cathode hybrid intake structure design and control for integrated hydrogen energy utilization system

Shihao Zhu [a], Hongming Hu [a], Banghua Du [b,**], Xinyu Lu [c], Yang Li [d], Changjun Xie [b,e,*], Leiqi Zhang [f], Bo Zhao [f]

[a] *School of Automation, Wuhan University of Technology, Wuhan, 430070, China*
[b] *Hubei Key Laboratory of Advanced Technology for Automotive Components, Wuhan University of Technology, Wuhan, 430070, China*
[c] *School of Energy and Power Engineering, Huazhong University of Science and Technology, Wuhan, 430074, China*
[d] *Department of Electrical Engineering, Chalmers University of Technology, Gothenburg, 41258, Sweden*
[e] *Wuhan Institute of Artificial Intelligence and New Energy Automobile Industry Technology, 11 Wuhan, 430070, China*
[f] *State Grid Zhejiang Electric Power Research Institute, Hangzhou, 310014, China*

ARTICLE INFO

Handling editor: A. Olabi

Keywords:
Proton exchange membrane fuel cell
Hybrid intake system
Fuzzy PID
Integrated hydrogen energy utilization system
Energy efficiency

ABSTRACT

The typical Integrated Hydrogen Energy Utilization System (IHEUS) does not recycle oxygen. For maximizing the system's efficiency, this study proposes a method for recycling byproduct oxygen in a Fuel Cell (FC) hybrid cathode intake structure and its control. By introducing the pure oxygen produced as a byproduct of hydrogen production into the FC, a hybrid cathode intake structure is formed with the air branch. To control this structure, models of the oxygen and air branch, and the FC stack are established. Subsequently, using BiLSTM network to learn historical data and extract relevant features, the output power demand of the FC system is predicted. Based on the prediction results, the required gas flow is calculated, and a fuzzy PID control strategy is employed to adjust the opening of the solenoid valve to change the gas flow to meet the demand. Finally, comparative studies show that our FC system, operating in a pure oxygen state, outperforms conventional air intake design: heat production increases by 13 %, electric efficiency improves by 20 %, and pure water savings reach 65.57 %. The air compressor witnesses a substantial 37.63 % reduction in power consumption, contributing to an overall energy efficiency increase of 8.92 % for the IHEUS.

Nomenclature

		e	Electron
		T	Temperature
Subscripts and superscripts		v-l	Vapor to liquid phase
		d-v	Dissolution to vapor
cp	Compressor	p	Power
atm	Atmosphere	Symbols	
trans	Transmit		
v	Vapor	W	Mass flow, kg/s
hm	Humidifier	p	Pressure, Pa
sat	Saturation	n	Rotate speed, RPM
a	Air	T	Temperature, K
pv	Pressure-reducing valve	Q	Heat, kJ
max	Maximum	C	Specific heat capacity, J/(kg•K)
p	Proportion	M	Molar mass, kg/mol

(*continued on next column*)

(*continued*)

i	Integration	U	Relative humidity, dimensionless
d	Differentiation	v	flow velocity, m/s
FC	Fuel cell	m	Mass, kg
ele	Electrical	n_i	Amount of substance i, mol
sys	System	S	Source term, kg/(m^3•s), mol/(m^3•s), A/(m^3•s) or W/m^3
FC_aux	Auxiliaries in fuel cell	EW	Equivalent weight of membrane
re	Recycle	J	Volumetric reaction rate, A/m^3
ex	Exergy	LHV	Low heating value, 242 kJ/mol
com	Compressor	R	Gas constant, 8.314 J/(mol•K)
g	Gas	Greek Symbols	
i	Gas species		
l	Liquid phase	τ	Time constant
mem	Membrane	γ	Air specific heat ratio
ion	Ionic	η	Efficiency

(*continued on next page*)

---

* Corresponding author. Hubei Key Laboratory of Advanced Technology for Automotive Components, Wuhan University of Technology, Wuhan, 430070, China.
** Corresponding author.
E-mail address: jackxie@whut.edu.cn (C. Xie).

https://doi.org/10.1016/j.energy.2024.132853
Received 19 April 2024; Received in revised form 24 June 2024; Accepted 15 August 2024

(*continued*)

eff	Effective value	ω	Oscillation frequency
mw	Membrane water	ζ	Damping factor

1. Introduction

In recent years, increased research efforts have been devoted to developing highly efficient and cost-effective clean energy conversion and utilization systems [1], among which hydrogen-to-electricity systems have attracted widespread attention due to the high energy density of hydrogen and the wide range of applications [2,3].

Hydrogen is available from a wide range of sources, and renewable energy for electrolysis of water to produce 'green hydrogen' is receiving increasing attention today. However, hydrogen transportation over long distances is expensive and poses severe safety risks [4]. These problems can be avoided by integrating hydrogen production and fuel cell (FC) power generation into an integrated hydrogen energy utilization system (IHEUS). In order to optimize the performance of IHEUS, Dong et al. [5] introduced an enhanced scene tree algorithm to realize reductions in energy expenses, demonstrating resilience when contrasted with the conventional scene tree algorithm. Similarly, Wu et al. [6] introduced an enhanced particle swarm optimization algorithm to optimize the operational parameters of components within a hydrogen energy system, with which the economic aspects and carbon reduction potential were also investigated. Yue et al. [7] mentioned in their overview that hydrogen energy devices can provide grid voltage support, and particularly, FCs can be one of the most important devices for local voltage regulation. Okundamiya [8] created the optimal involved architecture through HOMER's energy balancing methodology, which resulted in a 41 % savings in energy costs and a 3.308 % return on investment. In the existing research on IHEUS, most studies focus more on enhancing the system performance by adjusting the system operating conditions. In conventional IHEUS, all the oxygen from electrolytic hydrogen production is emitted to the environment, and the oxygen required for FC cathode fuel is recaptured from the air. Recycling this oxygen improves the efficiency of the system, so it is essential to propose a new structure to utilize this oxygen.

The factors that influence the performance of FCs are widely studied for designing new FCs. For example, Shen et al. [9] developed an anode-optimized active recirculation system, demonstrating its superior hydrogen utilization and system efficiency over other architectures. Yue et al. [10] investigated the effect of the distribution of hydrophobic streaks in the gas diffusion layer (GDL) on the performance of the FC using X-ray. Deng et al. [11] proposed an integrated PEMFC-PSA oxygen generation system and explored the effects of oxygen concentration, temperature, oxygen flow rate, and pressure on system efficiency and net power. Carcadea et al. [12] examined the effect of some key parameters of the porous layer on the performance of the FC stack and confirmed the importance of the porous layer. Chen et al. [13] developed an algorithm to optimize oxygen concentration under different operating conditions, providing a theoretical basis for designing PEMFC systems for residential hydrogen storage systems. Cheng et al. [14] reviewed the advantages of operating PEMFCs with pure oxygen compared to other air-independent propulsion (AIP) technologies. They found that PEMFC with H_2–O_2 can achieve higher power density and lower operational noise. The above studies indicate that enriched oxygen conditions can positively contribute to improving FC efficiency. This conclusion provides the theoretical basis for the work of this study. However, the aforementioned studies focus on oxygen-rich conditions rather than pure oxygen conditions. Therefore, this study also needs to verify the impact of pure oxygen on fuel cell performance.

The new structure has led to the proposal of corresponding control methods. For example, Daud et al. [15] mentioned that classical feedback and feedforward control with Proportional-Integral-Derivative (PID) controllers are the most commonly used control types to achieve better fuel cell performance. Wu et al. [16] reviewed control strategies for FC systems at both the system level and under different objectives, and briefly introduced integrated schemes for various applications. Yuan et al. [17] proposed a nonlinear internal state observer to monitor the oxygen and nitrogen content within the cathode of FC systems, thereby achieving adaptive adjustment of the cathode oxygen content. Chen et al. [18] introduced a Cascaded Internal Model Control (CIMC) method, which was experimentally validated to have good response speed, accuracy, and robustness. Liu et al. [19] proposed an anode purge scheme aimed at improving hydrogen utilization and protecting the stack of FC systems. Pei et al. [20] developed a lumped parameter model for shut-down purging using Simulink and innovatively proposed an open-loop control mechanism to adjust the purge flow rate. They conducted a detailed analysis of the proposed strategy by controlling variables to evaluate the operational variables affecting purge performance. The aforementioned studies have proposed control schemes from various aspects such as the overall stack and system components, aiming to enhance FC system performance. It can be observed that for a newly proposed fuel cell structure, corresponding control strategies can effectively help improve its performance.

To realize the proper and efficient utilization of oxygen, the improvement of the FC intake system is essential. The intake system is an important subsystem in the FC system, which regulates gas flow rate and humidity, thereby influencing FC performance. There are several studies on the optimization of intake systems. For example, Zhang et al. [21,22] designed a cathode cycling system to limit the high potentials that occur during startup and shutdown so as to reduce the hazard to the stack life. Chen et al. [23] built an FC system consisting of a stack and an air supply system, and they analyzed the effects of air excess ratio and air pressure on the voltage dynamic performance and net output power of the FC system. Yu et al. [24] replaced the hydrogen path injector with a miniature speed-adjustable peristaltic pump to study the effect of flow rate on the FC performance. Sun et al. [25] presented a coordinated control strategy for a high-power FC air supply system. The approach can significantly improve the efficiency of the air compressor, and at the same time, the FC has a short response time and excellent capability to follow the reference power. Chen et al. [26] designed a cathode field with multiple inlets fed in parallel to mitigate some of the undesirable effects caused by the linear depletion of the reaction gas. Gu et al. [27,28] investigated the dynamic characteristics of a claw-type hydrogen pump for fuel cells using a three-dimensional transient computational fluid dynamics (CFD) model. They conducted a multi-objective study of six factors affecting the pump performance, and the accuracy in predicting the pump performance using a proposed neural network analysis method was experimentally verified. Although improving the structure of the intake system can effectively increase the FC efficiency, most existing solutions with enriched oxygen do not directly utilize the oxygen produced by the hydrogen production system. This ignorance motivates us to propose an FC intake structure that can directly use the oxygen by-products from the hydrogen production system, thereby improving the energy efficiency of the IHEUS. The proposed FC cathode hybrid intake structure utilizing byproduct oxygen utilizes the oxygen produced by the hydrogen production system. Firstly, a Bidirectional Long Short-Term Memory (BiLSTM) network is employed to predict the power generation demand of the FC system at the next time step. Secondly, a fuzzy PID controller is used to control the opening of the intake valve, thereby changing the gas flow rate and achieving changes in the output power of the FC. Finally the system's feasibility is verified by analyzing the energy efficiency, auxiliary power consumption, and exergy of the FC power generation system. The novelties of this paper will be presented in the following points.

1) Unlike traditional cathodic air intake models, we proposed a novel structure that harnesses the by-product oxygen of the hydrogen production system and introduces inventive operation modes and

control strategies. It enables the fuel cell's oxygen and air modes to switch seamlessly when oxygen is in short supply.

2) Utilizing a CFD model of the FC stack, our findings verified that an increase in oxygen concentration significantly enhances FC performance, and it peaks in pure oxygen. This discovery offers unique insights for the development of pure oxygen FC designs.
3) A BiLSTM network is designed to predict the required output power of the FC system and realize the output power following to improve the system stability. And a fuzzy PID controller is implemented to regulate the valve actions to improve the fast response of the system.
4) Considering the possibility of insufficient oxygen supply, thus designing the dynamic switching of air intake and oxygen intake modes. This not only reduces energy consumption but also minimizes water consumption. This operational enhancement contributes to an overall boost in the system's energy efficiency.

The rest of the paper is structured as follows. Section 2 presents the detailed structure of the proposed FC intake system and the development of its mathematical model. Section 3 describes the control strategy and the execution module of the system. Section 4 introduces a semi-physical simulation platform for verifying the improved intake system and the control method. The main findings are concluded in Section 5.

2. System description and model development

In addressing the challenge of ineffective collection and utilization of oxygen produced by the hydrogen production system in the IHEUS, this study proposes a hybrid cathode intake structure for the FC system as schematized in Fig. 1. Hydrogen and oxygen obtained from the hydrogen production system are purified and dried into a storage tank, which is used as a source of PEMFC intake gas.

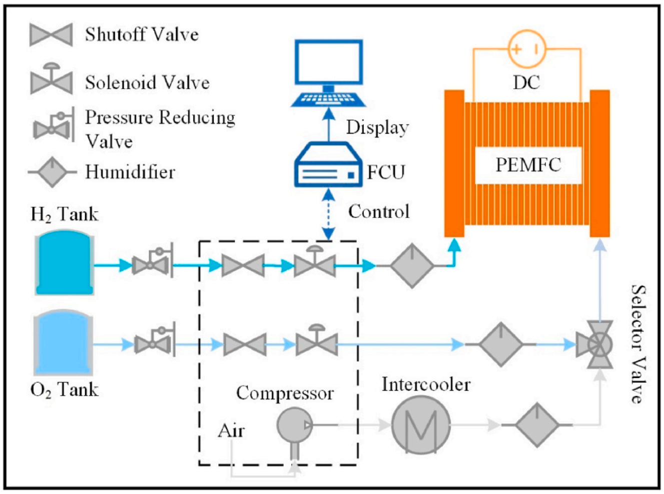

Fig. 2. Schematic diagram of the improved FC intake system.

The specific structure of the PEMFC power generation system is shown in Fig. 2. The hydrogen, originating from the hydrogen storage tank (HST), is directed into the anode of the FC by way of components. These include the pressure-reducing valve, which regulates hydrogen pressure, the shut-off valve for control, the solenoid valve enabling precise flow modulation, and the humidifier for optimizing moisture levels. The conventional PEMFC cathode intake system consists of an air compressor, an intercooler, and a humidifier. Of these components, the air compressor significantly contributes to the power consumption [29]. Therefore, the proposed intake system aims to reduce the air compressor frequency. The added OST branch doesn't require the addition of a compressor in the new branch because the oxygen output by the electrolyzer is at high pressure, similar to hydrogen. However, the pressure required for FC oxygen consumption is much lower than this pressure. This means that no additional energy consumption will be incurred in the new branch. The relevant parameters of the components involved in this study are shown in Table 1. The proposed cathode intake system consists of an oxygen branch and an air branch. The oxygen branch is similar to the anode, while the air branch retains its original structure. The two branches finally pass through a selector valve to the FC cathode. At the same time, the shut-off valves, solenoid valves, and air compressor in the anode intake and oxygen branch are controlled by the FC control unit (FCU), and the working conditions of the valves and air

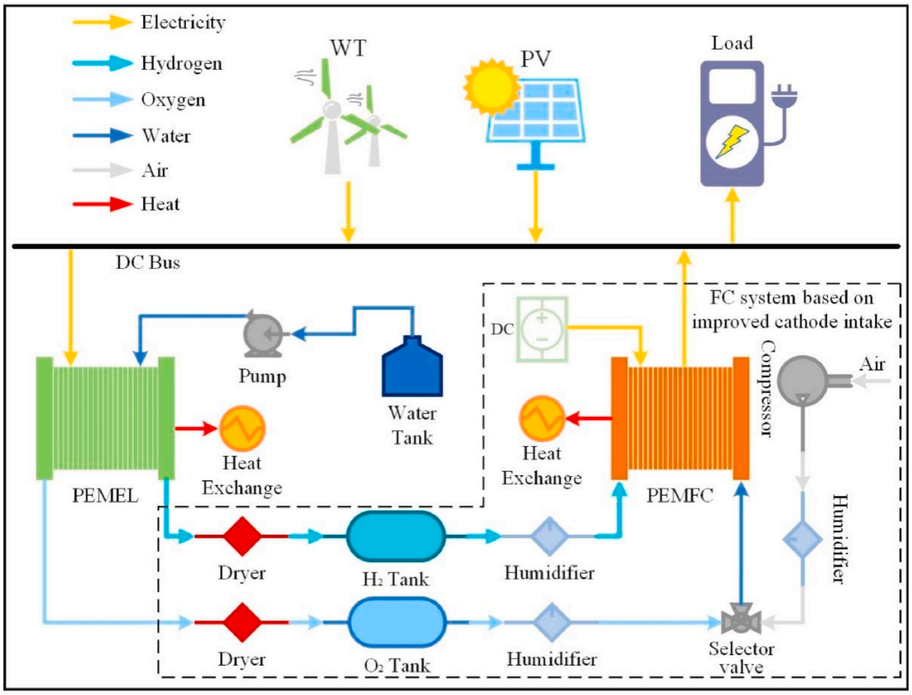

Fig. 1. Schematic diagram of IHEUS.

Table 1
Pressure parameters for different devices.

Devices	Parameters
Electrolyzer	Anode pressure(O_2): 2.8 MPa Cathode pressure(H_2): 3 MPa
Fuel cell	Anode pressure(H_2): 0.3 MPa Cathode pressure: (Air) 0.15 MPa, (O_2 partial pressure) 0.03 MPa
HST	3 MPa
OST	3 MPa

compressor are displayed in the upper computer.

2.1. Air branch

The main components of the air branch include three parts: air compressor, intercooler, and humidifier, and their mathematical models are shown as follows.

2.1.1. Compressor

By inputting environmental parameters and the air compressor speed, the air compressor's output flow rate W_{cp} is determined using a 3D lookup table or map depicted in Fig. 3. This relationship can be described as [30].

$$W_{cp} = f\left(n, \frac{p_{cp}}{p_{atm}}\right) \tag{1}$$

where n is air compressor speed, p_{cp} is air compressor outlet pressure, and p_{atm} is air compressor inlet pressure.

Considering the air compressor inertia, the dynamic process of the air compressor can be described as a first-order inertial system:

$$n_{real}(s) = \frac{1}{\tau s + 1} n_{set}(s) \tag{2}$$

where n_{real} is the air compressor's actual speed, n_{set} is the required air compressor speed, and τ is the time constant. A typical value of τ is 0.3 s.

Assuming the adiabatic operation of the air compressor, the outlet temperature of the air compressor T_{cp} is

$$T_{cp} = T_{atm}\left[1 + \frac{\left(p_{cp}/p_{atm}\right)^{\frac{\gamma-1}{\gamma}} - 1}{\eta_{cp}}\right] \tag{3}$$

where T_{atm} is the ambient temperature, considered equal to the air inlet temperature of the compressor, γ is the air-specific heat ratio, and η_{cp} is the compressor efficiency, which can be obtained in Fig. 3.

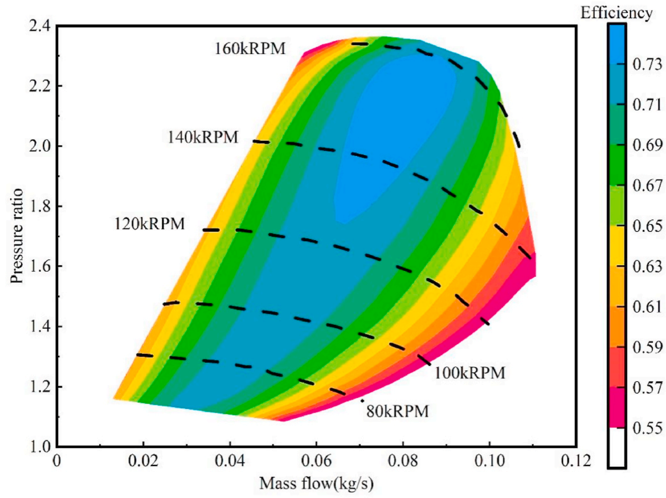

Fig. 3. Air compressor map.

2.1.2. Intercooler

Assuming that the intercooler is a variable temperature thermostat device, the intercooler outlet temperature can be expressed by

$$T_{cool} = T_{cp} - \frac{Q_{trans,cool}}{m_{cp} C_{air}} \tag{4}$$

where C_{air} is the air heat capacity and $Q_{trans,\ cool}$ is the heat transferred in the intercooler.

2.1.3. Humidifier

Assuming that the humidifier is a thermostatic device and the relative humidity of the gas after humidification is U, the mass flow rate $W_{v,\ hm}$ at the outlet of the humidifier can be calculated by

$$W_{v,hm} = \frac{M_v p_{sat} U W_{a,in}}{M_a p_{a,in}} \tag{5}$$

where p_{sat} is the saturated vapor pressure of water at the current temperature, U is the relative humidity set by the humidifier, $W_{a,in}$ is the mass flow rate of dry air entering the humidifier, M_v and M_a are the molar mass of water vapor and air, respectively, and $p_{a,in}$ is the pressure of dry air entering the humidifier.

2.2. Oxygen branch

The oxygen branch is equipped with diverse valves and humidifiers. Among them, the pressure-reducing valve solely adjusts the gas pressure as it passes through. Subsequently, the outlet flow rate v_{pv} of the pressure-reducing valve is

$$v_{pv} = \frac{p_{in}}{p_{pv}} v_{in} \tag{6}$$

where p_{in} and p_{pv} are the pressure-reducing valve inlet and outlet pressures, respectively, and v_{in} is the pressure-reducing valve inlet flow rate.

The dynamics of the solenoid valve can be approximated as a second-order dynamic system by

$$\frac{d^2y}{dt^2} + 2\omega\zeta\frac{dy}{dt} + \omega y = \omega^2 u \tag{7}$$

where u is the valve control signal, ω is the oscillation frequency of the valve, ζ is the damping coefficient of the valve, and y is the valve opening.

The actual output flow rate of the solenoid valve is related to the maximum flow rate that the solenoid valve can supply, given by

$$W = \begin{cases} 0 & y \le 0 \\ yW_{max} & 0 < y \le 1 \\ W_{max} & y > 1 \end{cases} \tag{8}$$

where W and W_{max} are the actual and maximum flow rates at the solenoid valve outlet, respectively.

The structure of the oxygen branch humidifier is the same as that of the air branch.

2.3. PEMFC stack

A high-fidelity 3-D CFD model of PEMFC was used to verify the impact of oxygen content on FC performance and assess the influence of an improved intake system on stack performance [31]. The CFD model contains conservation equations for mass, momentum, species, pressure, charge, and energy. The continuity and the Navier-Stokes equations describe airflows considered laminar due to the low Reynolds number.

Gas species conservation equations are used for hydrogen, oxygen, water vapor, and nitrogen. Separate liquid pressure conservation was added to describe liquid water transport in the GDL, the microporous layer (MPL), and the catalyst layer (CL), which are homogeneous porous media. The GDL considers anisotropic electrical and thermal conductivity in the in-plane and through-plane directions. The membrane water retention equation describes the water transfer in the membrane and CL. The transport of electrons and protons is governed by the equations for the conservation of electric and ionic charges. The energy conservation equation predicts the temperature distribution in the stack. The exact modeling process is shown in Appendix A. Table A1 lists the conservation equations, and Table A2 lists the corresponding source terms shown in Table A1 [32]. The feasibility verification and polarization characteristic curves of the model will be provided later.

3. Operation strategy

3.1. Power prediction

The startup of the FC system involves a time-lapse from the initiation command to reaching the required power output. This delay can result in a power imbalance in the grid, posing a potential threat to its stability [33]. Incorporating power prediction into the system allows the stacks to initiate ahead of the power demand point, ensuring timely response to grid requirements. The ability to predict power enhances the stability and reliability of the grid. Due to the typical correlation between predicted and historical data, intelligent algorithms that combine current information with historical data are best for power predictions [34]. Recurrent neural network (RNN) algorithms are one of the methods that can accommodate dependencies between successive time steps [35,36]. Hochreiter and Schmidhuber [37] proposed a long-short-term memory (LSTM) neural network, a special class of RNN. It can effectively solve the problem of gradient explosion or gradient disappearance, which is more likely to occur during the training process of primitive RNNs [38]. To further improve the accuracy of LSTM, Graves and Schmidhuber [39] proposed the BiLSTM network, which is one of the most widely used LSTM models [40]. For wind, solar and electrical load forecasting, long-term and periodicity are the main characteristics of this power data. Compared to other power forecasting algorithms, BiLSTM can more effectively capture the long-term dependencies of wind, solar and electrical load in time series, and its flexible model structure allows for adjustments and optimizations based on different climatic features, resulting in more accurate forecasting results [41].

BiLSTM processes forward- and backward-ordered data using two independent LSTM networks, as shown in Fig. 4. Each LSTM cell has three gates controlling the flow of information: An input gate, an output gate, and a forget gate. The forward LSTM processes the sequence from beginning to end, while the backward LSTM processes the sequence from end to beginning, and then connects the outputs of the two networks to produce the final prediction.

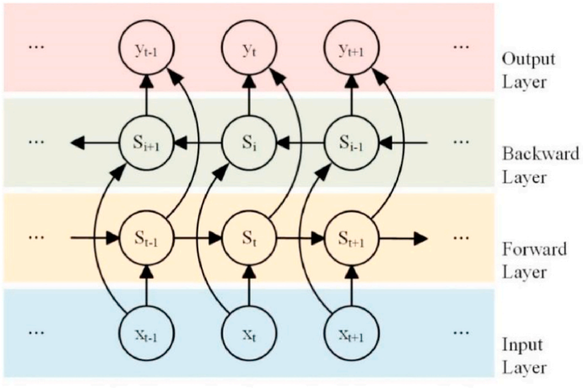

Fig. 4. BiLSTM structural topology.

In this study, the specific steps of using BiLSTM to predict wind-solar power generation and electricity load curves are as follows.

Step 1. Data Analysis and Preprocessing

Define the delay step k_{im} and prediction span z_{im}, partition the data into training set P_{train} and test set P_{test}, and normalize the data.

Step 2. Build BiLSTM Network Model

Set optimization algorithms (used to update weight matrix W and bias vector B) and configure model parameters.

Step 3. Train and Evaluate the Model

Define training parameters, use the trained model to predict P_{train} and P_{test}, obtaining P_{sim1} and P_{sim2}.

Step 4. Performance Evaluation

Calculate metrics such as mean absolute error (MAE), mean squared error (MSE), coefficient of determination (R^2) between P_{train} and P_{sim1}, P_{test} and P_{sim2}.

Step 5. Output Results

Output predicted results P_{sim1} and P_{sim2} along with their performance metrics.

3.2. Fuzzy PID control

When the FC is working, the gas discharged from the tank passes through three types of valves before entering the humidifier. The flow rate of the gas is directly influenced by the aperture of the solenoid valve. Therefore, precise and rapid control of the solenoid valve's opening benefits the stack reaction. Typically, a PID control is employed for regulating the solenoid valve. However, the parameters of the conventional PID controllers are fixed, making it challenging to fulfill the dynamic, nonlinear, and highly volatile control requirements of the FC system under a wide range of operating conditions. To address this challenge, many scholars have integrated fuzzy control, artificial intelligence algorithms, and other methods into PID control. The operation principle of the solenoid valve is simple, and the computational burden for control parameter calculation is small, which means that the adopted control strategy does not need to deal with a large amount of computation. Compared to most AI-based PID controllers, fuzzy PID controllers have a smaller computational burden, which enables faster operation for FC systems, thus meeting the real-time requirements of the system.

In summary, this study adopts the fuzzy PID control method. Fuzzy reasoning is applied to tuning the parameters of the PID controller, improving both the dynamic and steady-state performance of the valve control system. The approach facilitates accurate control and fast response of the solenoid valve, overcoming limitations associated with the fixed PID control parameters.

The structure of the solenoid valve fuzzy PID controller is shown in Fig. 5. In the designed fuzzy control system, the goal of controlling the solenoid valve opening is to regulate the gas release flow rate from the storage tank, requiring precise and rapid adjustments. The valve opening deviation *e* is determined by comparing the actual valve opening,

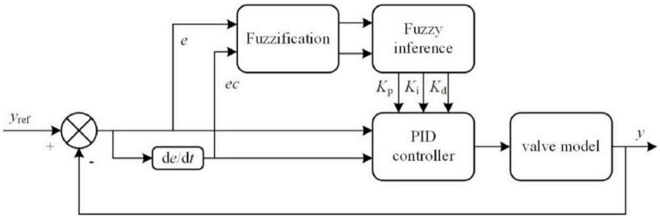

Fig. 5. Flow chart of fuzzy PID control.

detected by the solenoid valve position sensor, with the system set value. The fuzzy PID controller takes the valve opening deviation *e* and its rate of change *ec* as control inputs, and produces corrections to the PID gains ΔK_p, ΔK_i, and ΔK_d as control outputs. The flow rate is adjusted by feedback of the valve opening signal, with the reference value set to the theoretical valve opening corresponding to the gas demand. Traditional PID controllers, with fixed parameters, cannot adapt to the proposed structure and scenario conditions, as the fuel cell intake system must adjust to complex working conditions and variable intake valve openings.

The five variables *e*, *ec*, K_p, ΔK_i, and K_d were converted into seven fuzzy variables {NB, NM, NS, ZO, PS, PM, PB} representing negative large, negative medium, negative small, zero, positive small, positive medium and positive large, respectively. The corresponding fuzzy inference rules are given in Appendix B. We set the domains of the five variables *e*, *ec*, K_p, ΔK_i, and K_d to {-1, 2, 5, 8, 11, 14, 17}, {-15, −12.16, −9.336, −6.5, −3.669, −0.833, 2}, {-1.5, −1, −0.5, 0, 0.5, 1, 1.5}, {-0.1, 0, 0.1, 0.2, 0.3, 0.4, 0.5} and {-0.1, −0.667, −0.033, 0, 0.033, 0.667, 0.1}.

3.3. Hybrid intake control

The PEMFC anode intake is provided by the HST, and the proposed cathode intake control is shown in Fig. 6.

In this control strategy, first, historical power data of the system are obtained to predict the power of the next moment using the BiLSTM network. The working status of the electrolyzer/fuel cell is determined based on the predicted net power being positive or negative. If the net power is negative, the fuel cell starts working to supply electricity to the microgrid. The required amount of oxygen is calculated based on the power prediction and the optimal stoichiometry at that current. and compared to the maximum oxygen release rate from the oxygen storage tank (OST). This rate is related to the amount of oxygen stored in the OST. Oxygen release will be inhibited or even stopped when there is not enough oxygen. If the oxygen demand is below the pipeline rate limit, the PEMFC operates in pure oxygen mode, with the air branch of the cathode intake system inactive. If the demand exceeds the pipeline limit, the OST shut-off valve closes, activating the air compressor, and the PEMFC operates under air conditions.

The optimal excess oxygen ratio under different currents in the power-gas curve in the figure is provided by Table 2 [42].

Table 2
Optimal oxygen excess ratio under different current.

Current(A)	Optimal oxygen excess ratio
60	2.91
80	2.75
100	2.44
120	2.33
140	2.2
160	2.13

3.4. Performance evaluation parameters of the system

In this study, the overall performance of the PEMFC system with

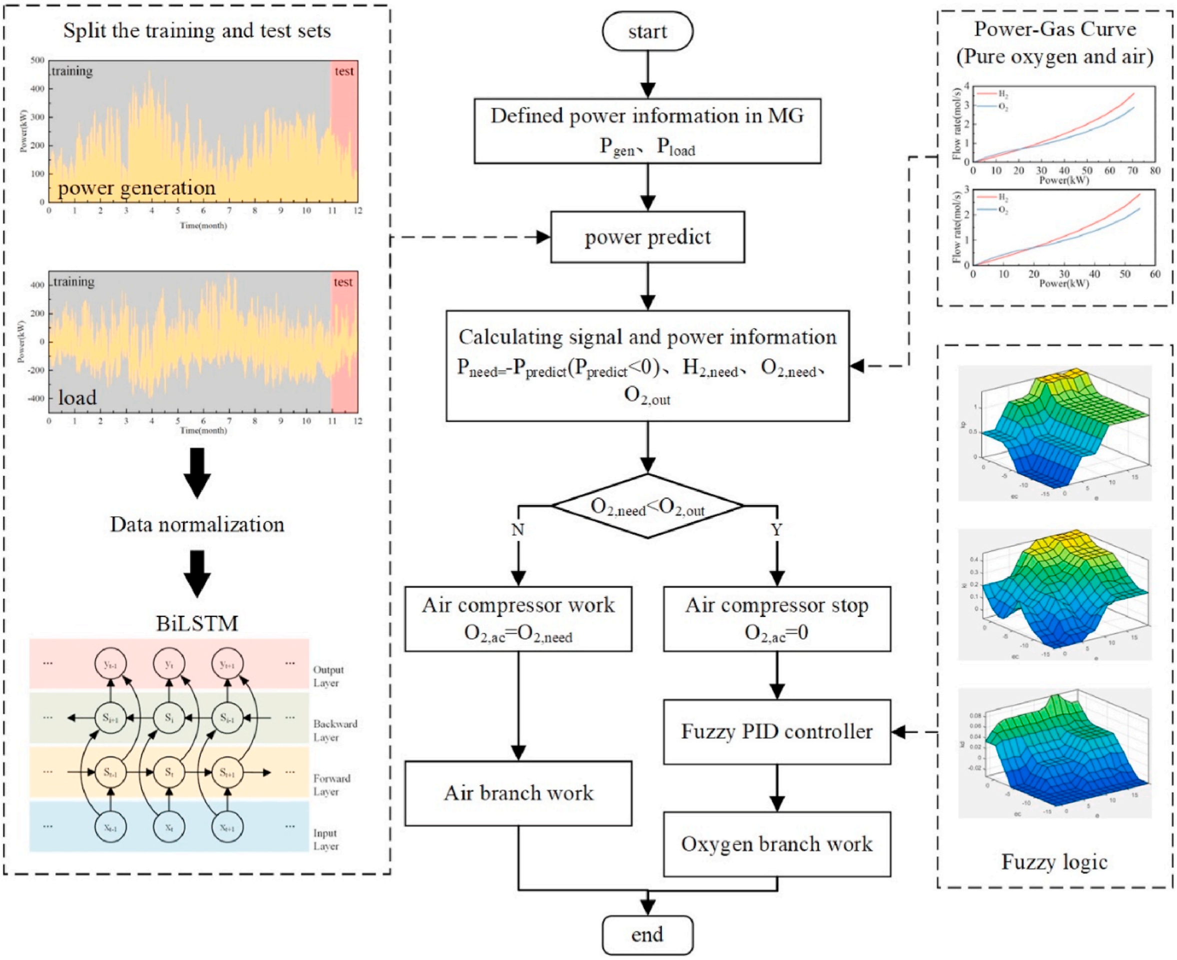

Fig. 6. Flow chart of PEMFC cathode intake control.

hybrid cathode intake is evaluated through four metrics: PEMFC hydrogen-electric conversion efficiency, system energy efficiency, system exergy efficiency, and water consumption. They are defined by

$$\eta_{FC\_ele} = \frac{W_{FC}}{n_{H_2} \cdot LHV} \tag{9}$$

$$\eta_{FC\_sys} = \frac{W_{FC} - W_{FC\_aux} + Q_{re}}{n_{H_2} \cdot LHV} \tag{10}$$

$$\eta_{FC\_ex} = \frac{W_{FC} - W_{com}}{m_{H_2} \cdot ex_{H_2} - Q_{re}} \tag{11}$$

$$\begin{cases} n_{H_2O} = (pV)/(RT) \\ RH = p/p_{sat} \\ p_{sat} = -1.69 \times 10^{-7} T^4 + 3.85 \times 10^{-4} T^3 - 3.39 \times 10^{-4} T^2 + 0.143T - 20.9 \end{cases} \tag{12}$$

where W_{FC} is the fuel cell power output, n_{H_2} is the amount of substance of hydrogen consumed, LHV is the low calorific value of hydrogen with a value of 242 kJ/mol, W_{FC_aux} is the auxiliary power consumption of the FC system, Q_{re} is the heat recovered by the system, W_{com} is the electrical energy consumed by the air compressor, m_{H_2} is the mass of hydrogen consumed, and ex_{H_2} is the standard chemical exergy of hydrogen. Furthermore, p, V, and T denote the pressure, volume, and temperature of the water vapor used for humidification, respectively, R is the ideal gas constant, and p_{sat} is the saturated vapor pressure.

4. Result and discussion

4.1. Introduction of simulation platform

To validate the proposed structure and control strategy, the presented system model and control algorithm were implemented in an FC hardware-in-the-loop (HIL) platform shown in Fig. 7. The FC HIL includes a power management module, a low-voltage programmable power source, a Siemens industrial computer, a 90 pin standard board chassis, an NI real-time simulation system, and a PowerECU controller. The Siemens industrial computer was mainly used to debug and compile the PEMFC system simulation model and build the PowerECU control model by MATLAB. The model was deployed to the NI real-time simulation system through Veristand, which monitors the signals and manages the startup and operation of the NI real-time simulation system. The NI real-time simulation system uses the PEMFC model to calculate the sensor voltage and CAN communication signals. It receives PowerECU control signals, providing the advantage of simulating real operating conditions.

Table 3
Geometry parameters and operation conditions.

Parameters	Value
Mesh thickness (mm)	0.15
Mesh saddle width (mm)	0.6
Length of mesh saddle slope (mm)	0.3
Mesh saddle plane contact (mm)	0.4
Electrode thickness (mm)	0.2
Membrane thickness (mm)	0.05
Cooling plate thickness (mm)	0.075
Cooling channel height (mm)	0.6
Inlet temperature (°C)	70
Relative humidity	0.85
Inlet flow rate (m/s)	Anode: 0.1; Cathode: 0.5

4.2. Model validation

4.2.1. Effect of oxygen enrichment on fuel cell performance

In order to examine the impact of oxygen concentration on the PEMFC performance, we will first validate the established stack model. Subsequently, the stack performance tests will be conducted under varied oxygen contents, employing specific geometric parameters and operating conditions as detailed in Table 3.

The simulation for validating the established PEMFC stack model was carried out by selecting the conditions that the cathode intake is air

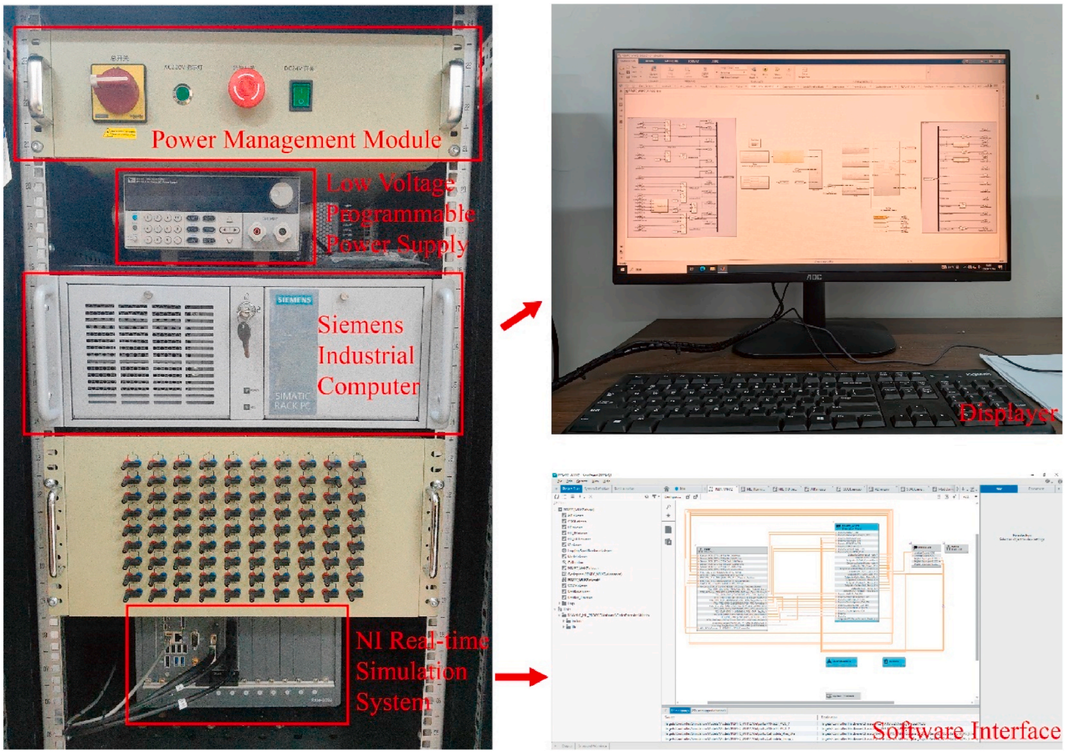

Fig. 7. HIL system structure for fuel cells and operating interface.

and the initial temperature of the stack was 70 °C. The obtained results were compared with those of Chugh et al. [43], and the results are shown in Fig. 8. It can be seen that the PEMFC stack model established in this study is close to the actual data, with the maximum absolute error below 0.05 V.

After verifying the model, the effect of oxygen concentration on FC performance is further examined. The oxygen concentrations were tested at the following levels: 21 % (Air), 30 %, 40 %, 50 %, 60 %, 70 %, 80 %, 90 %, and 100 % (pure oxygen). The relative humidity of the gas entering the cathode was 85 %. The results obtained are shown in Figs. 9 and 10.

Fig. 9 shows the polarization voltage and power obtained by passing different oxygen concentrations to the FC cathode. It can be seen that both the FC polarization voltage and the power reach their lowest values when air is fed into the stack. As the oxygen concentration rises, the polarization voltage also increases, which means that consuming the same mass of hydrogen produces more electricity. The peak polarization voltage and the maximum output power of the stack are attained when the stack is supplied with pure oxygen. The rate of redox reactions in an electric reactor is related to the concentration of reactants. Therefore, a higher concentration of oxygen, acting as a cathodic reactant, enhances its effective participation in electrochemical reactions, thereby minimizing energy losses. In addition, as the oxygen concentration increases, the polarization voltage loss of the stack decreases, consequently boosting the stack power. Therefore, in the cathode intake system, the passage of pure oxygen as cathode fuel can effectively improve the FC efficiency.

In Fig. 10, the variations in stack temperature and heat generation are depicted for different oxygen concentrations supplied to the cathode. The change in stack temperature when the air is energized is minimal. As the oxygen concentration increases, the operating temperature of the FC also rises, leading to a substantial increase in the stack heat output. This is because as the oxygen concentration increases, the electrochemical reaction rate between hydrogen and oxygen accelerates. This results in more hydrogen reacting with oxygen, releasing more energy. A portion of this energy is released in the form of heat, so with higher oxygen concentration, the heat generation of the stack also increases. Therefore, using pure oxygen as the cathode fuel effectively enhances the FC's thermal efficiency in the FC cathode intake system.

In summary, supplying air with higher oxygen concentration (or even pure oxygen) to the FC cathode is an effective measure to improve the FC performance.

4.2.2. *Performance of fuzzy PID controller*

The control effect of fuzzy PID for solenoid valves was verified by setting up three groups of comparison experiments: A reference group, a PID control group, and a fuzzy PID control group. During the validation process, the oxygen demand generated by load changes in the FC system is converted into changes in valve opening. This conversion not only makes the validation results more intuitive but also better reflects the system's response under actual working conditions. By monitoring and adjusting the valve opening, the oxygen supply can be timely adjusted to meet the system's demand, thereby achieving stable operation and efficient performance of the FC system. All three experiments were configured with two processes: From fully closed to fully open and vice versa, yielding the results shown in Fig. 11.

Fig. 12 compares the performance of different control strategies based on the results obtained from Fig. 11. Traditional PID control achieves a 0.06 s lead in solenoid valve response time. However, it results in an 8.29 % increase in overshoot, which may be detrimental to the valve's operation. In comparison, the fuzzy PID control not only advances the response time by 0.46 s but also reduces the overshooting to 3 %. This presents a significant improvement, reducing the level of

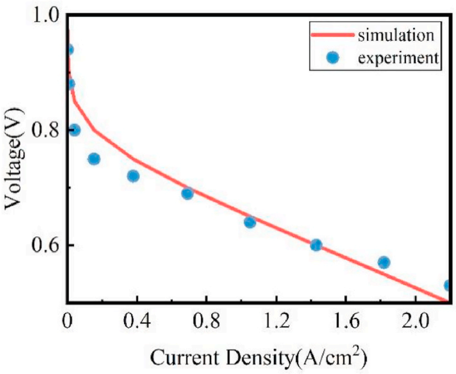

Fig. 8. Comparison of experimental and modeling polarization curve.

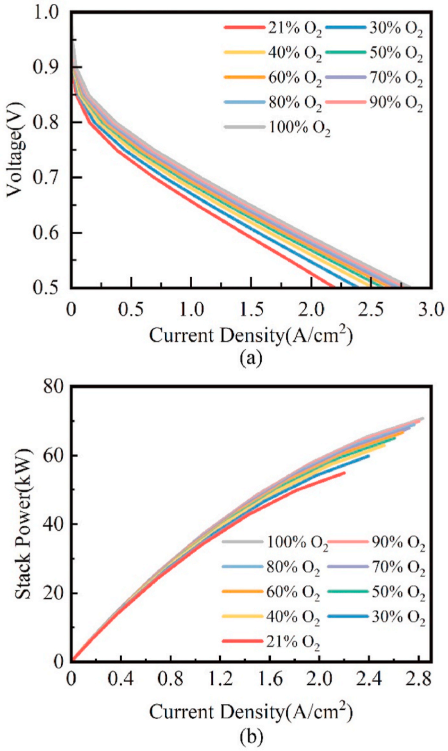

Fig. 9. Polarization curves under different oxygen concentration conditions(a) voltage; (b)power.

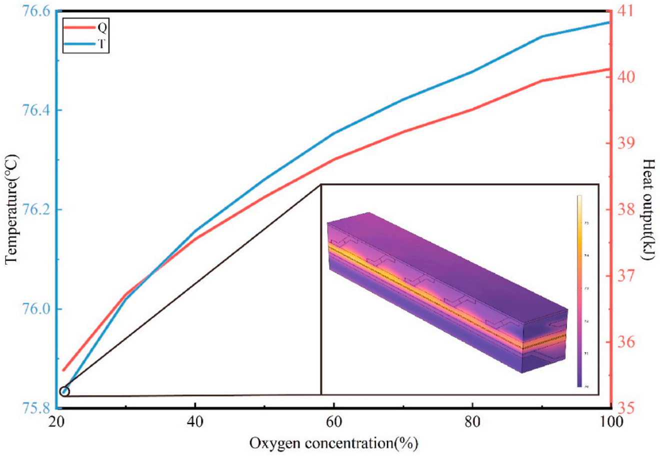

Fig. 10. Temperature change under different oxygen concentration conditions.

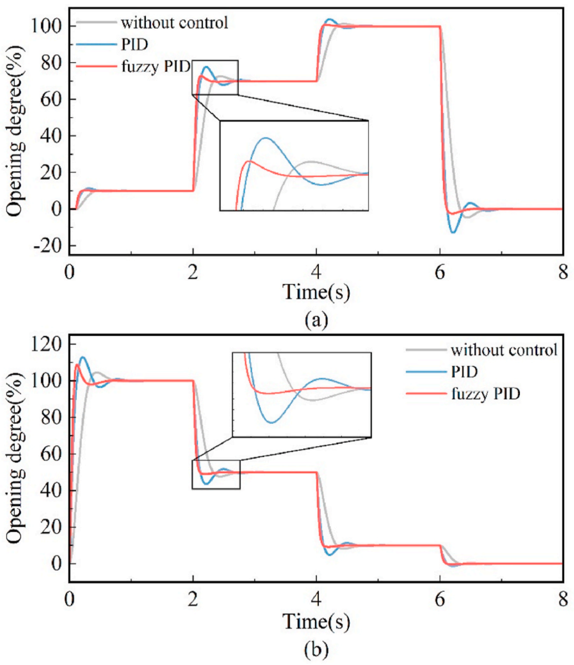

Fig. 11. Comparison curves of the valve opening degree (a) opening procedure; (b) closing procedure.

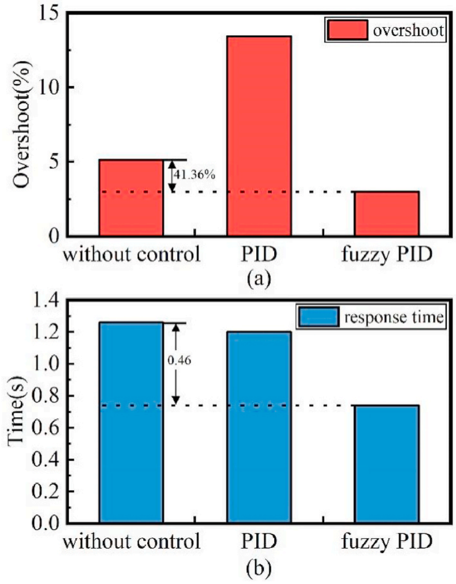

Fig. 12. Comparison of control performance in terms of (a) overshoot and (b) response time.

overshooting by 41.63 % and 77.66 % and enhancing the response speed by 41.26 % and 38.33 % compared to the original response and the traditional PID control, respectively. The fuzzy PID controller dynamically adjusts the control parameters (ΔK_p, ΔK_i, ΔK_d) based on real-time feedback, allowing for quicker adaptation to changes in valve position. This results in a faster response time as the system can promptly react to deviations from the setpoint. The fuzzy PID control system provides more nuanced adjustments by considering both the deviation *e* and the rate of change *ec*. This leads to smoother transitions and minimizes the risk of overshooting, thereby protecting the valve from excessive wear and tear. The fuzzy PID controller's ability to adaptively modify the control gains ensures a more precise and efficient response to system changes. This adaptability is particularly beneficial in scenarios where the fuel cell intake system must adjust to varying working conditions and gas demands. The continuous adjustment of control parameters in fuzzy PID control allows the system to compensate for external disturbances and internal variations more effectively than traditional PID control, which relies on fixed parameters. Consequently, the proposed fuzzy PID control demonstrates fast response speed, high steady-state accuracy, and strong anti-interference capability, making it a more effective solution for regulating the solenoid valve in the integrated hydrogen energy utilization system (IHEUS), especially under off-grid conditions with fluctuating demands.

4.2.3. *Output performance of cathode inlet*

In order to verify the feasibility of the proposed PEMFC cathode intake system and its control strategy, three sets of control experiments were conducted, with the experimental parameters given in Table 4.

The current was varied within three equally spaced curves ranging from 50 A to 200 A. To enhance the illustration of the effectiveness of the control strategy, different initial oxygen flow rates were employed to keep the oxygen content in the OST within a fluctuating range. The simulation duration is set to 10 h, and the resulting curve obtained is shown in Fig. 13.

Figs. 13(a–1)(b-1)(c-1) shows the operating currents. The associated relationship between the oxygen required by the FC cathode intake system and the supply calculated from the real-time gas stored in the oxygen tank is shown in Figs. 13(a-2)(b-2)(c-2). The proposed control strategy switches the intake path according to the relationship between the oxygen content in the OST and the required oxygen, as shown in Figs. 13(a-3)(b-3)(c-3), which verifies the effectiveness of the proposed structure and control strategy.

4.3. *Case study*

To further validate the designed system architecture, simulations will be conducted in this section using actual generation and load power data as input conditions.

4.3.1. *Hardware-in-the-loop simulation*

The IHEUS is a form of renewable energy microgrid application and an extension technology of the main power grid, effectively addressing the problem of the high electricity cost in remote areas. Additionally, its capability to operate in an off-grid mode enhances resilience against natural disasters [44]. However, evaluating the system's reliability requires a long test period. Therefore, selecting the appropriate data size is essential.

In this study, the dataset spans an entire year, with the data from the first 11 months serving as the training set and the data from the last month as the test set. This selection ensures that 1) the test data encompasses most of the fluctuating behaviors of the wind, solar, and load and 2) the forecasting model is universally suitable for long-term forecasting. The predicted wind, solar, and load profiles of 720 h are obtained and compared with the real values in Figs. 14 and 15.

As shown in Fig. 14(a) and (b), the prediction results have some errors with the real values due to the uncertainty of wind and solar resources. As shown in Fig. 14(c), the prediction accuracy obtained is further improved after integrating wind and photovoltaic power generation data and then forecasting. As shown in Fig. 15, the prediction results have less error with the real value because the load fluctuation is

Table 4
Experimental parameter.

No.	Current variation range (A)	OST input flow rate (mol/s)
1	50–100	0.01
2	100–150	0.02
3	150–200	0.024

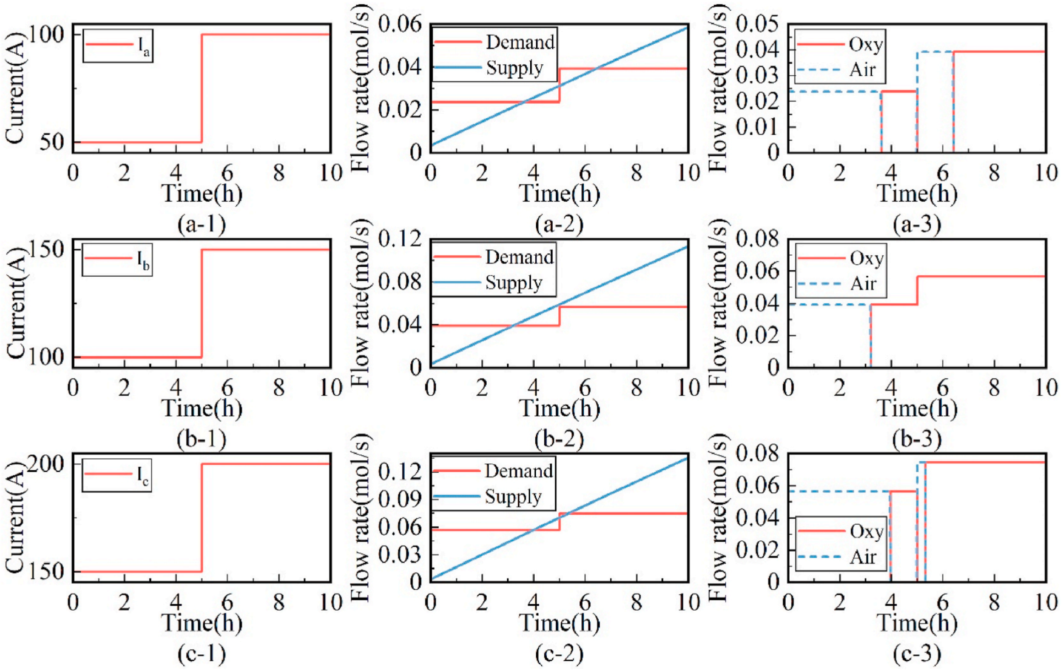

Fig. 13. Working state of the cathode intake system at different test currents (a) curve at 50–100 A; (b) curve at 100–150 A; (c) curve at 150–200 A.

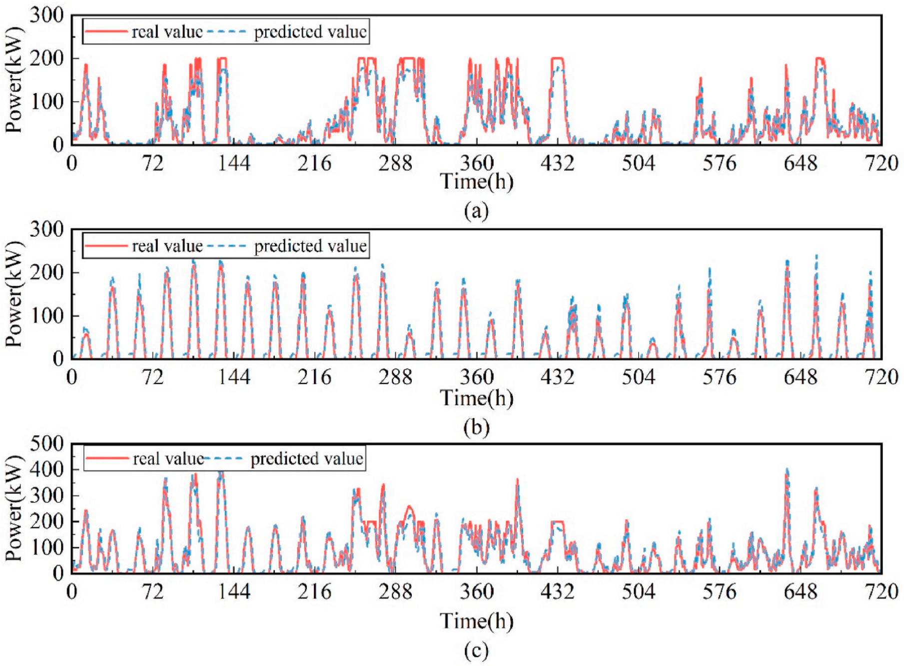

Fig. 14. Comparison of predicted and actual data of (a) wind power, (b) solar power, and (c) combined wind and solar power.

small and more regular. The excellent performance of the predictor is indicated as follows: The mean absolute percentage error (MAPE) is 1.38 %, the root mean square error (RMSE) is 7.00, and the coefficient of determination (R^2) is 0.99. In summary, using the BiLSTM network can accurately predict the power fluctuation in the system and provide a theoretical basis for improving the system response speed.

Therefore, 168 h of the predicted power data above were selected as input data to generate Figs. 16 and 17. Fig. 16 illustrates the stable operation of the modified cathode intake system's oxygen and air branches under the power conditions shown in Fig. 16(a) and with the proposed control strategy shown in Fig. 16(b). For a more intuitive representation of the operation of the oxygen branch circuit, Fig. 16(c) depicts the fluctuation curve of the oxygen storage volume over the 168 h test environment. As can be seen in Fig. 16(c), the oxygen in the OST fluctuates as the FC oxygen branch alternates with the air branch. Moreover, the high oxygen content helps to release oxygen quickly.

In Fig. 17(a), it is evident that the improved PEMFC consumes about 17.24 kg of hydrogen, making a 12.35 % reduction compared to the 19.67 kg consumed by the conventional intake mode. Furthermore, Fig. 17(b) illustrates a significant reduction in the electrical energy consumed by the air compressor in the improved cathode intake system, decreasing from 304.3 kJ to 189.8 kJ. This represents a considerable

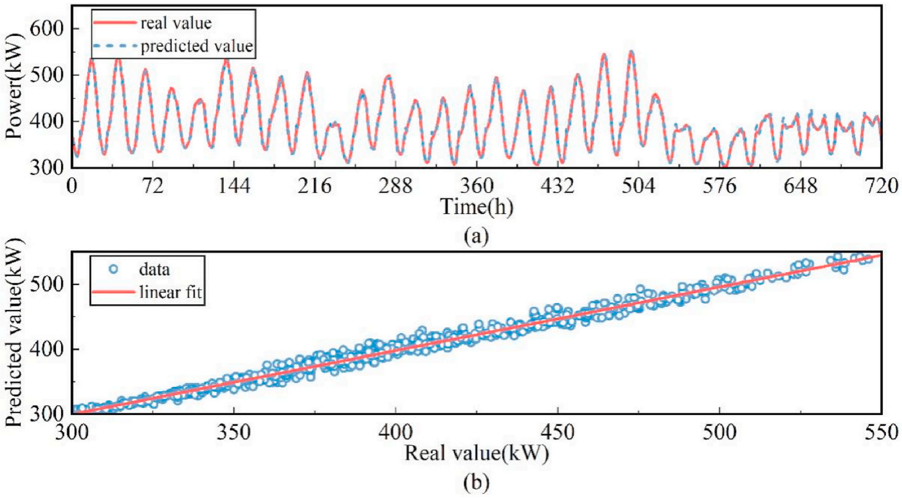

Fig. 15. Load (a) comparison of test results; (b) rendering of the test set.

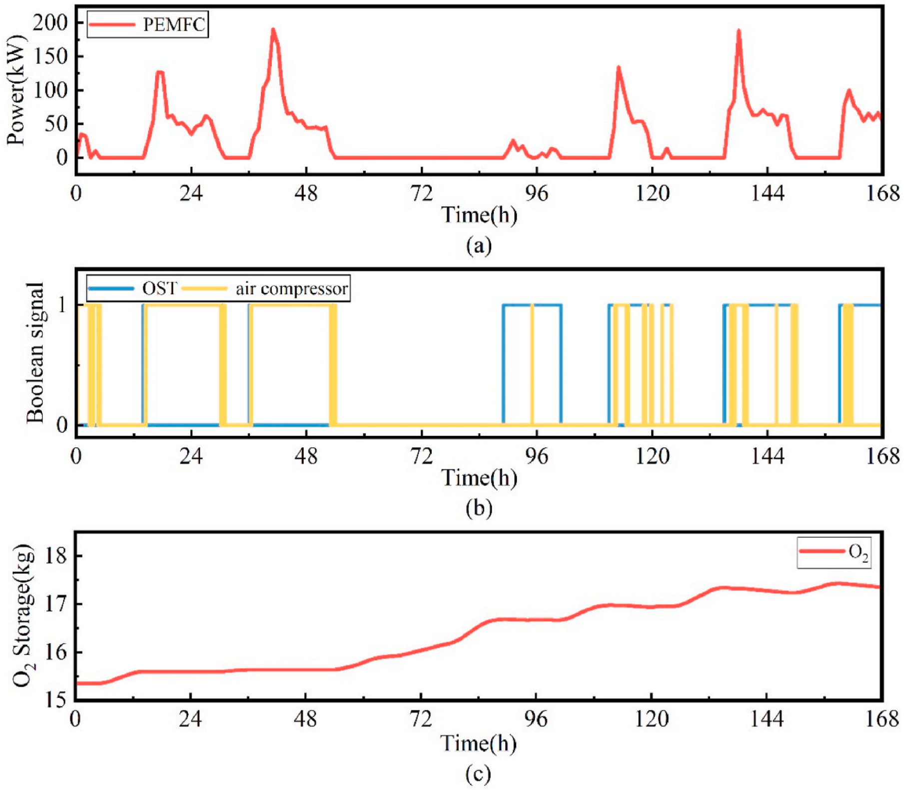

Fig. 16. PEMFC system test results (a) input power; (b) oxygen branch and air branch working signals; (c)amount of stored oxygen.

energy saving of about 37.63 % compared to the conventional cathode intake system.

Based on the results in Figss. 16 and 17, gas consumptions at different power levels were calculated and shown in Figs. 18 and 19. The average hydrogen-to-electricity conversion efficiency of the FC system was 52.02 %, the average energy efficiency was 96.87 %, and the average exergy efficiency was 45.87 % following a 168 h operation under actual input conditions. The average efficiencies of the system with conventional structure were 45.60 %, 80.32 %, and 34.98 %, which were improved by 4.62 %, 16.55 %, and 10.89 %, respectively. The overall energy efficiency of IHEUS saw an enhancement from 43.29 % to 52.21 %.

4.3.2. *Analog simulation*

The stability and feasibility of the system under dynamic working conditions were verified in 4.3.2. To further test the system performance, the following operational test of the system under steady state conditions is carried out. Using a PEMFC with a rated power of 120 kW as an example, operate it steadily at power levels of 12 kW, 30 kW, 60 kW, 90 kW, and 120 kW for a period of time. The tests include measuring the oxygen consumption under pure oxygen and air intake conditions within a unit of time, as well as the amount of pure water required for humidification under both working conditions. Different from the validation experiment, to test the humidification water consumption under different intake conditions while maintaining the same humidity level, the relative humidity of pure oxygen needs to be increased to 100 %,

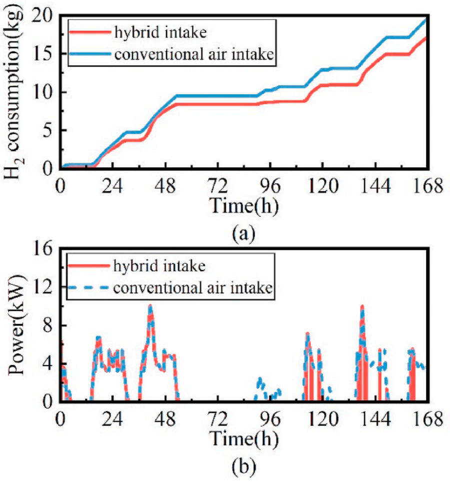

Fig. 17. Comparison result (a)H$_2$ consumption; (b)power consumption of air compressor.

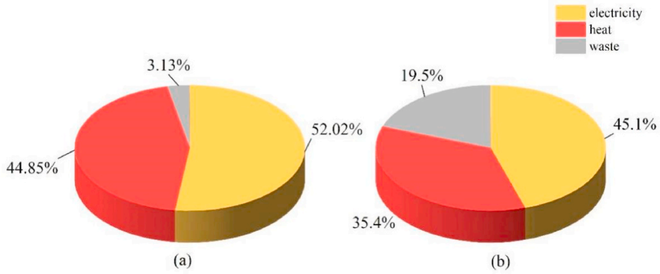

Fig. 18. Average efficiency under 168 h working conditions of (a) the hybrid intake subsystem and (b) the conventional air intake subsystem.

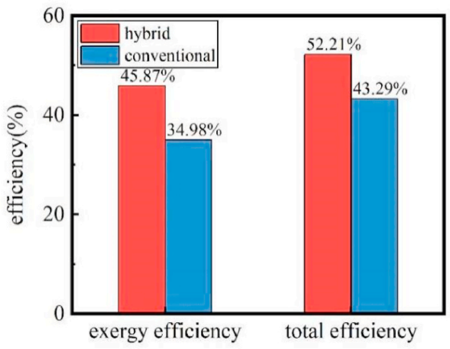

Fig. 19. Comparison of system efficiency.

while air only needs to be increased to 50 % [45]. The results are shown in Fig. 20.

As the power of the PEMFC increases, the difference in the required oxygen between pure oxygen and air intake also increases. Compared to pure oxygen, the air intake introduces a large amount of non-fuel gases, which hinders the contact between oxygen and the electrode, thereby reducing the reaction rate. Additionally, when air is introduced to the cathode, the gas flow rate increases, resulting in higher pure water consumption to maintain the set relative humidity during humidification. In contrast, using pure oxygen can significantly reduce the need for pure water, lowering the water consumption from 0.61 mol/s to 0.21 mol/s, i.e., a reduction of 65.57 % of the water consumption.

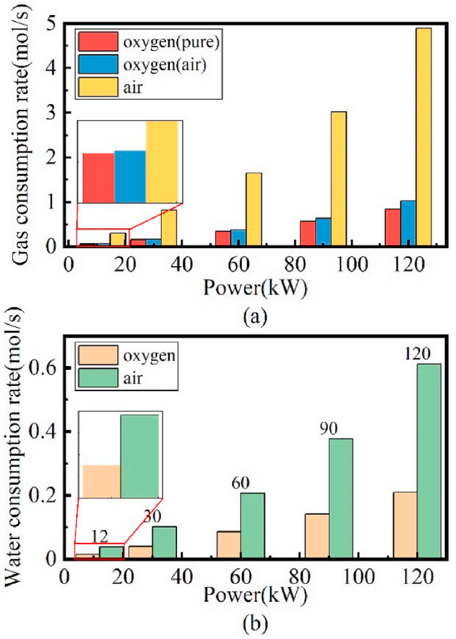

Fig. 20. Gas consumption at different powers (a) amount of air intake; (b) amount of water required for humidification.

5. Conclusion

To address the issue of oxygen underutilization in the IHEUS, this study proposes a hybrid cathode intake system that recycles byproduct oxygen. Firstly, based on the traditional fuel cell (FC) cathode intake structure, an oxygen branch is added to recycle the byproduct oxygen, and models for the cathode oxygen branch, air branch, and FC stack are established. Through multi-physics coupling simulations, the impact of changes in oxygen concentration on FC performance is verified. To realize mixed intake control, historical data features are learned using a BiLSTM network to predict future trends in wind and solar power generation, calculate the required power output of the FC, and determine the required gas flow. Simultaneously, a fuzzy PID controller is used to control the opening of the solenoid valve to adjust the gas flow and achieve adaptive power generation according to the demand of the FC. Finally, under 168 h of off-grid operating conditions, the system's performance is validated against the specified indicators using hardware-in-the-loop simulation platforms. The main concluding remarks are given as follows.

1) As the concentration of oxygen increases, the power of the FC rises, and the power in the state of pure oxygen is increased by about 20 % compared to the power in the state of air. Elevated oxygen concentrations also lead to higher heat production in the stacks, with pure oxygen increasing by about 13 % compared to air.
2) The proposed fuzzy PID controller improves the 0.46 s response of the solenoid valve and reduces the overshoot by 41.63 %, thus improving the control of the intake system. The air intake control strategy can respond to the real-time status of the system and judge the working conditions of the air branch and oxygen branch according to the power demand. The oxygen branch is the main working condition, and the air branch is the auxiliary operating condition.
3) On the real-time simulation platform, the air compressor saves about 37.63 % of power after 168 h of operation under test conditions. The average hydrogen-electric conversion efficiency of the FC system was 52.02 %, the average energy efficiency was 96.87 %, and the average exergy efficiency was 45.87 %. Compared to the traditional structure, the improvement was 4.62 %, 16.55 %, and 10.89 %,

respectively. The IHEUS is highly efficient by 8.92 %. When operating at rated power, the system saves about 65.57 % water.

In summary, introducing oxygen at the cathode significantly enhances both the hydrogen-to-electricity conversion efficiency and the heat generation compared to traditional intake methods. Additionally, using a fuzzy PID controller to control the valve opening results in noticeable improvements in response speed and control accuracy over a conventional PID controller. Finally, a 168-h operation test verified the applicability of the mixed intake structure in IHEUS. Compared to the traditional PEMFC operation in IHEUS, the PEMFC with the mixed intake structure demonstrates superior performance.

It is important to note that while introducing pure oxygen does enhance FC performance, it also increases heat generation significantly, posing a considerable challenge for the FC cooling system. In future work, we will further analyze the variations in heat generation and design corresponding cooling circuits to achieve precise temperature control of the FC.

CRediT authorship contribution statement

Shihao Zhu: Writing – original draft, Software, Investigation, Data curation. **Hongming Hu:** Resources, Methodology. **Banghua Du:** Validation, Formal analysis. **Xinyu Lu:** Visualization, Data curation. **Yang Li:** Writing – review & editing, Resources. **Changjun Xie:** Writing – review & editing, Supervision, Funding acquisition, Conceptualization. **Leiqi Zhang:** Validation, Project administration. **Bo Zhao:** Project administration, Conceptualization.

Declaration of competing interest

The authors declare that they have no known competing financial interests or personal relationships that could have appeared to influence the work reported in this paper.

Data availability

Data will be made available on request.

Acknowledgement

This work was supported by the National Key Research and Development Program of China (No. 2020YFB1506802) and the Key Research and Development Project of Guangdong Province (2020B0909040004).

Appendix A

Table A1
Conservation equations

Descriptions	Equations
Mass(gas)	$\frac{\partial}{\partial t}(\varepsilon(1-s)\rho_g)+\nabla\cdot(\rho_g u_g)=S_m$
Momentum(gas)	$\frac{\partial}{\partial t}\left[\frac{\rho_g u_g}{\varepsilon(1-s)}\right]+\nabla\cdot\left[\frac{\rho_g u_g^2}{\varepsilon^2(1-s)^2}\right]=-\nabla P_g-\frac{2}{3}\mu_g\nabla\left\{\nabla\cdot\left[\frac{u_g}{\varepsilon(1-s)}\right]\right\}+\mu_g\nabla\left\{\nabla\cdot\left[\frac{u_g}{\varepsilon(1-s)}\right]+\nabla\cdot\left[\frac{u_g^T}{\varepsilon(1-s)}\right]\right\}+S_u$
Species(gas)	$\frac{\partial}{\partial t}[\varepsilon(1-s)\rho_g Y_i]+\nabla\cdot(\rho_g u_g Y_i)=\nabla\cdot\left(\rho_g D_i^{eff}\nabla Y_i\right)+S_i$
Liquid pressure	$\frac{\partial}{\partial t}(\rho_l\varepsilon s)=\nabla\cdot\left(\rho_l\frac{Kk_l}{\mu_l}\nabla P_l\right)+S_l$
Membrane water	$\frac{\rho_{mem}}{EW}\frac{\partial}{\partial t}(\omega\lambda)+\nabla\cdot\left(n_d\frac{J_{ion}}{F}\right)=\frac{\rho_{mem}}{EW}\nabla\cdot\left(D_d^{eff}\nabla\lambda\right)+S_{mw}$
Electric potential	$0=\nabla\cdot\left(\kappa_e^{eff}\nabla\varphi_e\right)+S_e$
Ionic potential	$0=\nabla\cdot\left(\kappa_{ion}^{eff}\nabla\varphi_{ion}\right)+S_{ion}$
Energy	$\frac{\partial}{\partial t}\left[\varepsilon s\rho_l C_{p,l}T+\varepsilon(1-s)\rho_g C_{p,g}T\right]+\nabla\cdot\left[\varepsilon s\rho_l C_{p,l}u_l T+\varepsilon(1-s)\rho_g C_{p,g}u_g T\right]=\nabla\cdot\left(k^{eff}\nabla T\right)S_T$

Table A2
Source terms

Terms	Expressions
S_{H_2} (kg/(m^3•s))	$-M_{H_2O}\frac{J_a}{2F}$, ACL
S_{O_2} (kg/(m^3•s))	$-M_{H_2O}\frac{J_c}{4F}$, CCL
S_{H_2O} (kg/(m^3•s))	$\begin{cases}-S_{v-1} & \text{GDL, MPL}\\ -S_{v-1}+-S_{v-d} & \text{ACL}\\ -S_{v-1}+-S_{v-d}+M_{H_2O}J_c/2F & \text{CCL}\end{cases}$
S_g (kg/(m^3•s))	$\begin{cases}-S_{v-1}+S_{v-d}-J_aM_{H_2}/2F & \text{ACL}\\ -S_{v-1}+S_{v-d}-J_cM_{O_2}/4F & \text{CCL}\\ -S_{v-1} & \text{GDLs and MPLs}\end{cases}$
S_{v-l} (kg/(m^3•s))	$\begin{cases}\gamma_{v-1}\varepsilon(1-s)(C_{H_2O}-C_{sat})M_{H_2O} & C_{H_2O}>C_{sat}\\ \gamma_{1-v}\varepsilon s(C_{H_2O}-C_{sat})M_{H_2O} & C_{H_2O}<C_{sat}\end{cases}$
S_e (A/m^3)	$\left\{-J_aJ_c\ \begin{matrix}\text{ACL}\\ \text{CCL}\end{matrix}\right.$

(*continued on next page*)

Table A2 (*continued*)

Terms	Expressions
S_{ion} (A/m^3)	$\left\{ J_{\mathrm{a}} - J_{\mathrm{c}} \begin{array}{l} \text{ACL} \\ \text{CCL} \end{array} \right.$
S_{mw} (mol/(m^3•s))	$\begin{cases} -S_{\mathrm{d-v}}/M_{\mathrm{H_2O}} - S_{\mathrm{p}} & \text{ACL} \\ -S_{\mathrm{d-v}}/M_{\mathrm{H_2O}} + S_{\mathrm{p}} & \text{CCL} \end{cases}$
$S_{\mathrm{d-v}}$ (kg/(m^3•s))	$\gamma_{\mathrm{d-v}}\rho_{\mathrm{mem}}/\mathrm{EW}(\lambda - \lambda_{\mathrm{eq}})M_{\mathrm{H_2O}}$
S_{p} (mol/(m^3•s))	$\dfrac{\rho_1 K_{\mathrm{mem}}(\overline{P}_{\mathrm{la}} - \overline{P}_{\mathrm{lc}})}{\mu_1 M_{\mathrm{H_2O}}\delta_{\mathrm{mem}}\delta_{\mathrm{CL}}}$
S_{T} (W/m^3)	$\begin{cases} \lVert \nabla\varphi_{\mathrm{e}} \rVert^2 \kappa_{\mathrm{e}}^{\mathrm{eff}} & \text{ABP} \\ \lVert \nabla\varphi_{\mathrm{e}} \rVert^2 \kappa_{\mathrm{e}}^{\mathrm{eff}} + S_{\mathrm{v-l}}h & \text{GDLs, MPLs} \\ J_{\mathrm{a}}\lvert \eta_{\mathrm{act}}^{\mathrm{a}} \rvert + \lVert \nabla\varphi_{\mathrm{e}} \rVert^2 \kappa_{\mathrm{e}}^{\mathrm{eff}} + \lVert \nabla\varphi_{\mathrm{ion}} \rVert^2 \kappa_{\mathrm{ion}}^{\mathrm{eff}} + J_{\mathrm{a}}\dfrac{\Delta S_{\mathrm{a}} T}{2F} + (S_{\mathrm{v-l}} - S_{\mathrm{d-v}})h & \text{ACL} \\ J_{\mathrm{c}}\lvert \eta_{\mathrm{act}}^{\mathrm{c}} \rvert + \lVert \nabla\varphi_{\mathrm{e}} \rVert^2 \kappa_{\mathrm{e}}^{\mathrm{eff}} + \lVert \nabla\varphi_{\mathrm{ion}} \rVert^2 \kappa_{\mathrm{ion}}^{\mathrm{eff}} + J_{\mathrm{c}}\dfrac{\Delta S_{\mathrm{c}} T}{4F} + (S_{\mathrm{v-l}} - S_{\mathrm{d-v}})h & \text{CCL} \\ \lVert \nabla\varphi_{\mathrm{ion}} \rVert^2 \kappa_{\mathrm{ion}}^{\mathrm{eff}} & \text{Membrane} \\ S_{\mathrm{v-l}}h & \text{Flow fields} \end{cases}$

Appendix B

Table B1
Fuzzy control rule of K_{p}

e	ec						
	NB	NM	NS	ZO	PS	PM	PB
NB	PB	PB	PM	PM	PS	PO	PO
NM	PB	PB	PM	PS	PS	PO	NS
NS	PM	PM	PM	PS	ZO	NS	NS
ZO	PM	PM	PS	ZO	NS	NM	NM
PS	PS	PS	ZO	NS	NS	NM	NM
PM	PS	PS	NS	NM	NM	NM	NB
PB	ZO	ZO	NM	NM	NM	NB	NB

Table B2
Fuzzy control rule of K_{i}

e	ec						
	NB	NM	NS	ZO	PS	PM	PB
NB	NB	NB	NM	NM	NS	ZO	ZO
NM	NB	NB	NM	NS	NS	ZO	ZO
NS	NB	NM	NS	NS	ZO	PS	PS
ZO	NM	NM	NS	ZO	PS	PM	PM
PS	NM	NS	ZO	PS	PS	PM	PB
PM	ZO	ZO	PS	PS	PM	PB	PB
PB	ZO	ZO	PS	PM	PM	PB	PB

Table B3
Fuzzy control rule of K_{d}

e	ec						
	NB	NM	NS	ZO	PS	PM	PB
NB	PS	NS	NB	NB	NB	NM	PS
NM	PS	NS	NB	NM	NM	NS	ZO
NS	ZO	NS	NM	NM	NS	NS	ZO
ZO	ZO	NS	NS	NS	NS	NS	ZO
PS	ZO	ZO	ZO	ZO	ZO	ZO	ZO
PM	PB	NS	PS	PS	PS	PS	PB
PB	PB	PM	PM	PM	PS	PS	PB

References

[1] Koivunen T, Khosravi A, Syri S. The role of power–to–hydrogen in carbon neutral energy and industrial systems: case Finland. Energy 2023;284:128624.

[2] Song H, Liu Y, Bian H, Shen M, Lin X. Energy, environment, and economic analyses on a novel hydrogen production method by electrified steam methane reforming with renewable energy accommodation. Energy Convers Manag 2022;258:115513.

[3] Lu X, Du B, Zhu W, Yang Y, Xie C, Tu Z, Deng Z. Thermodynamic and dynamic analysis of a hybrid PEMFC-ORC combined heat and power (CHP) system. Energy Convers Manag 2023;292:117408.

[4] Kannaiyan K, Lekshmi GS, Ramakrishna S, Kang M, Kumaravel V. Perspectives for the green hydrogen energy-based economy. Energy 2023;284:129358.

[5] Dong Xiangxiang, et al. Optimal coordination of hydrogen-based integrated energy systems with combination of hydrogen and water storage. Appl Energy 2022;308:118274.

[6] Wu F, Gao R, Li C, Liu J. A comprehensive evaluation of wind-PV-salt cavern-hydrogen energy storage and utilization system: a case study in Qianjiang salt cavern, China. Energy Convers Manag 2023;277:116633.

[7] Yue M, Lambert H, Pahon E, Roche R, Jemei S, Hissel D. Hydrogen energy systems: a critical review of technologies, applications, trends and challenges. Renew Sustain Energy Rev 2021;146:111180.

[8] Okundamiya MS. Size optimization of a hybrid photovoltaic/fuel cell grid connected power system including hydrogen storage. Int J Hydrogen Energy 2021;46(59):30539–46.

[9] Shen KY, Park S, Kim YB. Hydrogen utilization enhancement of proton exchange membrane fuel cell with anode recirculation system through a purge strategy. Int J Hydrogen Energy 2020;45(33):16773–86.

[10] Yue L, Wang S, Araki T, Utaka Y, Wang Y. Effect of water distribution in gas diffusion layer on proton exchange membrane fuel cell performance. Int J Hydrogen Energy 2021;46(3):2969–77.

[11] Deng M, Zhang Q, Huang Y, Zhang X. Integration and optimization for a PEMFC and PSA oxygen production combined system. Energy Convers Manag 2021;236:114062.

[12] Carcadea E, Varlam M, Ismail M, Ingham DB, Marinoiu A, Raceanu M, Ion-Ebrasu D. PEM fuel cell performance improvement through numerical optimization of the parameters of the porous layers. Int J Hydrogen Energy 2020;45(14):7968–80.

[13] Chen F, Ye H, Pei Y. Optimizing the economic viability of proton exchange membrane fuel cells operated with oxygen-enriched cathode air for residential hydrogen energy storage systems. Int J Hydrogen Energy 2024;65:236–51.

[14] Cheng M, Liu M, Feng Y, Guo Y, Xu H, Luo L, Zhang J. Technical challenges and enhancement strategies for transitioning PEMFCs from H2-air to H2-O2. Energy Convers Manag 2024;311:118525.

[15] Daud WRW, Rosli RE, Majlan EH, Hamid SAA, Mohamed R, Husaini T. PEM fuel cell system control: a review. Renew Energy 2017;113:620–38.

[16] Wu D, Peng C, Yin C, Tang H. Review of system integration and control of proton exchange membrane fuel cells. Electrochem Energy Rev 2020;3:466–505.

[17] Yuan H, Dai H, Wei X, Ming P. A novel model-based internal state observer of a fuel cell system for electric vehicles using improved Kalman filter approach. Appl Energy 2020;268:115009.

[18] Chen F, Jiao J, Hou Z, Cheng W, Cai J, Xia Z, Chen J. Robust polymer electrolyte membrane fuel cell temperature tracking control based on cascade internal model control. J Power Sources 2020;479:229008.

[19] Liu Z, Chen J, Liu H, Yan C, Hou Y, He Q, Hissel D. Anode purge management for hydrogen utilization and stack durability improvement of PEM fuel cell systems. Appl Energy 2020;275:115110.

[20] Pei Y, Chen F, Jiao J, Liu S. Analysis and control strategy design for PEMFC purging process. Energy 2024;290:130233.

[21] Zhang Q, Tong Z, Tong S, Cheng Z. Self-humidifying effect of air self-circulation system for proton exchange membrane fuel cell engines. Renew Energy 2021;164:1143–55.

[22] Zhang Q, Tong Z, Tong S. Effect of cathode recirculation on high potential limitation and self-humidification of hydrogen fuel cell system. J Power Sources 2020;468:228388.

[23] Chen H, Liu Z, Ye X, Yi L, Xu S, Zhang T. Air flow and pressure optimization for air supply in proton exchange membrane fuel cell system. Energy 2022;238:121949.

[24] Yu X, Fan J, Zhou Y, Hao D, Chen J, Yu T, Zhang C. Experimental investigation of the effect of hydrogen recirculation on the performance of a proton exchange membrane fuel cell. Int J Hydrogen Energy 2022;47(2):1183–91.

[25] Sun T, Zhang X, Chen B, Liu X. Coordination control strategy for the air management of heavy vehicle fuel cell engine. Int J Hydrogen Energy 2020;45(39):20360–8.

[26] Chen D, Zou Y, Shi W, Serbin S, You H. Proton exchange membrane fuel cells using new cathode field designs of multi-inlet shunt intake design. Int J Energy Res 2021;45(7):9948–60.

[27] Gu P, Xing L, Wang Y, Feng J, Peng X. Transient flow field and performance analysis of a claw pump for FCVs. Int J Hydrogen Energy 2021;46(1):984–97.

[28] Gu P, Xing L, Wang Y, Feng J, Peng X. A multi-objective parametric study of the claw hydrogen pump for fuel cell vehicles using taguchi method and ANN. Int J Hydrogen Energy 2021;46(9):6680–92.

[29] Li Y, Pei P, Ma Z, Ren P, Huang H. Analysis of air compression, progress of compressor and control for optimal energy efficiency in proton exchange membrane fuel cell. Renew Sustain Energy Rev 2020;133:110304.

[30] Chen H, Liu Z, Ye X, Yi L, Xu S, Zhang T. Air flow and pressure optimization for air supply in proton exchange membrane fuel cell system. Energy 2022;238:121949.

[31] Macedo-Valencia J, Sierra JM, Figueroa-Ramírez SJ, Díaz SE, Meza M. 3D CFD modeling of a PEM fuel cell stack. Int J Hydrogen Energy 2016;41(48):23425–33.

[32] Zhang G, Yuan H, Wang Y, Jiao K. Three-dimensional simulation of a new cooling strategy for proton exchange membrane fuel cell stack using a non-isothermal multiphase model. Appl Energy 2019;255:113865.

[33] Alharbi AG, Olabi AG, Rezk H, Fathy A, Abdelkareem MA. Optimized energy management and control strategy of photovoltaic/PEM fuel cell/batteries/supercapacitors DC microgrid system. Energy 2024;290:130121.

[34] Gao M, Li J, Hong F, Long D. Day-ahead power forecasting in a large-scale photovoltaic plant based on weather classification using LSTM. Energy 2019;187:115838.

[35] Yu C, Li Y, Zhao L, Chen Q, Xun Y. A novel time-frequency recurrent network and its advanced version for short-term wind speed predictions. Energy 2023;262:125556.

[36] Duan J, Zuo H, Bai Y, Duan J, Chang M, Chen B. Short-term wind speed forecasting using recurrent neural networks with error correction. Energy 2021;217:119397.

[37] Hochreiter S, Schmidhuber J. Long short-term memory. Neural Comput 1997;9(8):1735–80.

[38] Dhaked DK, Dadhich S, Birla D. Power output forecasting of solar photovoltaic plant using LSTM. Green Energy and Intelligent Transportation 2023;2(5):100113.

[39] Graves A, Graves A. Long short-term memory. Supervised sequence labelling with recurrent neural networks; 2012. p. 37–45.

[40] Niu D, Sun L, Yu M, Wang K. Point and interval forecasting of ultra-short-term wind power based on a data-driven method and hybrid deep learning model. Energy 2022;254:124384.

[41] Wang FK, Mamo T, Cheng XB. Bi-directional long short-term memory recurrent neural network with attention for stack voltage degradation from proton exchange membrane fuel cells. J Power Sources 2020;461:228170.

[42] Chen J, Liu Z, Wang F, Ouyang Q, Su H. Optimal oxygen excess ratio control for PEM fuel cells. IEEE Trans Control Syst Technol 2017;26(5):1711–21.

[43] Chugh S, Chaudhari C, Sonkar K, Sharma A, Kapur GS, Ramakumar SSV. Experimental and modelling studies of low temperature PEMFC performance. Int J Hydrogen Energy 2020;45(15):8866–74.

[44] Prevedello G, Werth A. The benefits of sharing in off-grid microgrids: a case study in the Philippines. Appl Energy 2021;303:117605.

[45] Ozen DN, Timurkutluk B, Altinisik K. Effects of operation temperature and reactant gas humidity levels on performance of PEM fuel cells. Renew Sustain Energy Rev 2016;59:1298–306.